



APPLIED PHYSICS

Long-lived enhanced magnetization—A practical metabolic MRI contrast material

Itai Katz^{1*}, Asher Schmidt^{1†}, Ira Ben-Shir¹, Marcia Javitt², Karel Kouřil³, Andrea Capozzi^{4,5}, Benno Meier^{3,6}, Arad Lang⁷, Boaz Pokroy⁷, Aharon Blank^{1*}

Noninvasive tracking of biochemical processes in the body is paramount in diagnostic medicine. Among the leading techniques is spectroscopic magnetic resonance imaging (MRI), which tracks metabolites with an amplified (hyperpolarized) magnetization signal injected into the subject just before scanning. Traditionally, the brief enhanced magnetization period of these agents limited clinical imaging. We propose a solution based on amalgamating two materials—one having diagnostic-metabolic activity and the other characterized by robust magnetization retention. This combination slows the magnetization decay in the diagnostic metabolic probe, which receives continuously replenished magnetization from the companion material. Thus, it extends the magnetization lifetime in some of our measurements to beyond 4 min, with net magnetization enhanced by more than four orders of magnitude. This could allow the metabolic probes to remain magnetized from injection until they reach the targeted organ, improving tissue signatures in clinical imaging. Upon validation, this metabolic MRI technique promises wide-ranging clinical applications, including diagnostic imaging, therapeutic monitoring, and posttreatment surveillance.

INTRODUCTION

Magnetic resonance imaging (MRI) is a mainstream noninvasive medical imaging modality with excellent soft tissue contrast without ionizing radiation (1, 2). MRI uses physical properties of tissues such as proton density, relaxation rates, and diffusion coefficients to visualize anatomy for tissue characterization, extent of disease, surgical planning, treatment selection, and medical decision-making for the patients' benefit (3). However, conventional MRI has generally not capitalized on detection of various metabolites in the body that are important clinical markers of malignancy (4), stress (5), cell proliferation (6), or cell death (7) mainly because these metabolites are typically present at very low millimolar concentrations.

Hyperpolarization (HP) is a generic term describing a family of techniques devised to boost the nuclear magnetic resonance (NMR) signal, which is the basis for MRI data acquisition (8–14). The NMR signal is the result of an energy exchange between electromagnetic waves and the Zeeman energy levels of the magnetic moments of nuclei of interest, placed under a large static magnetic field. This signal is proportional to the so-called nuclear magnetic polarization, P_N [polarization is defined as $P_N = (N_\uparrow - N_\downarrow)/(N_\uparrow + N_\downarrow)$, where N_\uparrow is the population of the upper Zeeman energy level and N_\downarrow is the population of the lower level], which, without the HP boost, is at thermal equilibrium and amounts to ~10 parts per million (ppm) at most. This means that the other 99.999% of the sample is completely NMR silent. The objective of HP is to increase P_N from 10 ppm to

tens of percents, with a proportional gain in NMR signal. If a ^{13}C isotopically enriched material is used for metabolic HP applications, then two orders of magnitude more MRI-visible nuclei can be detected compared to natural materials. The net effect of both HP and ^{13}C enrichment is that the metabolite concentration appears more than six orders of magnitude larger than physiologically available, making spectroscopic MRI feasible.

Some HP techniques have been adopted into clinical practice, for example, optically pumped hyperpolarized Xe used in lung imaging (14–16). Others are still under development, such as HP using reactions with parahydrogen (17–19) or the use of photoexcited naphthalene as a source of polarization (20). Until now, the most robust, versatile, and clinically advanced HP technique is the dissolution dynamic nuclear polarization (dDNP) method (4, 9, 21–26). This technique is based on unpaired electrons (e.g., those found in stable free radicals or crystal defects) that have a much larger magnetic moment than ^{13}C nuclei and, at a magnetic field of 3 to 10 T, attain near-unity polarization when the temperature is lowered to ~1.5 K. In dDNP, a frozen solution of the metabolite of interest is prepared with a stable radical. By virtue of electron-nuclear interactions and irradiating the electron spin system near resonance, the high polarization native to the electron population can be transferred to the nuclear population (11, 12). Following a rapid dissolution process, the hyperpolarized nuclear spins can be detected at ambient conditions. A mechanistic description of the dDNP process is shown in Fig. 1.

Preclinical dDNP systems were introduced about two decades ago (27), followed shortly by a clinical system (25, 26). However, there has been very limited usage of the clinical system beyond the experimental phase. The reasons for that are diverse, as explained in this recent review (28) including the issue of measurement reproducibility: “Food and Drug Administration approval and clinical adoption of HP ^{13}C MRI will require establishing its clinical utility in subsequent larger phase II and III trials. Critical to this is the demonstration of reproducibility...” (28). We argue that the biggest barrier to the successful adoption of HP MRI has been the fact that the return of the hyperpolarized metabolite to equilibrium occurs too fast. The

¹Schulich Faculty of Chemistry, Technion—Israel Institute of Technology, Haifa 3200003, Israel. ²Rambam Medical Center, Haifa, Israel. ³Institute of Biological Interfaces 4, Karlsruhe Institute of Technology, Eggenstein-Leopoldshafen 76344, Germany. ⁴LIFMET, Institute of Physics, École Polytechnique Fédérale de Lausanne (EPFL), Station 6, 1015 Lausanne, Switzerland. ⁵HYPERMAG, Department of Health Technology, Technical University of Denmark, Building 349, 2800 Kgs Lyngby, Denmark. ⁶Institute of Physical Chemistry, Karlsruhe Institute of Technology, Karlsruhe 76131, Germany. ⁷Department of Materials Science and Engineering, Technion—Israel Institute of Technology, Haifa 3200003, Israel.

*Corresponding author. Email: ab359@technion.ac.il (A.B.); itaik2002@yahoo.com (I.K.)

†Deceased.

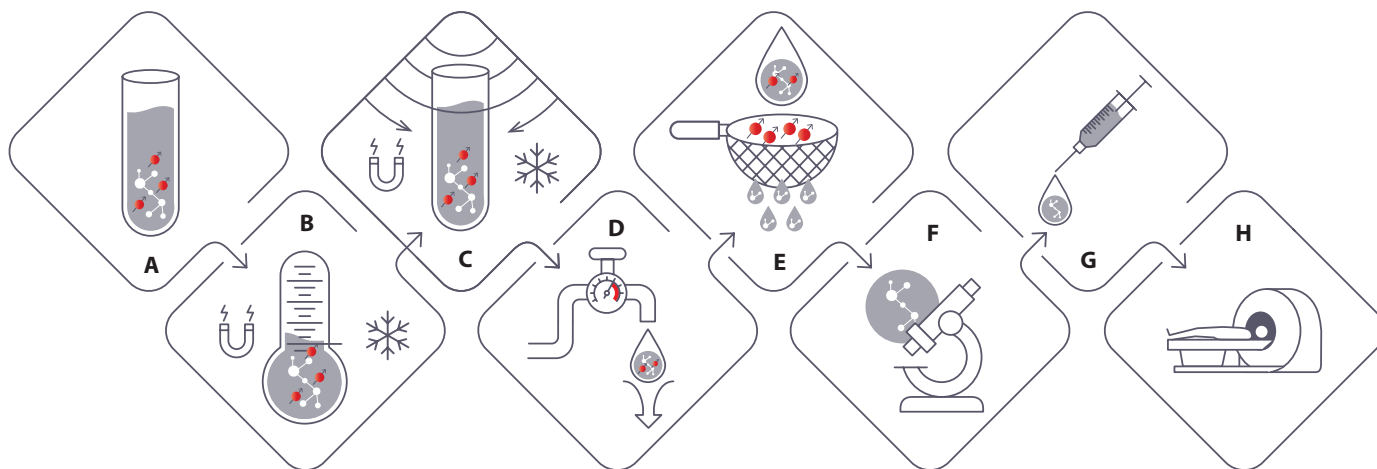


Fig. 1. A schematic illustration of a typical dDNP process. (A) The sample of interest (shown as a white molecule) is brought into contact with a spin bath of unpaired electrons (red spheres), usually by way of mixing it with a stable free radical or inducing free radicals to form in the sample itself. (B) The sample is then placed in a strong magnetic field and cooled to a temperature of approximately 1.5 K. (C) Under these conditions, it is microwave (MW)-irradiated near the electron Larmor frequency, causing polarization transfer to the nuclear spin bath. (D) Next, the sample is flushed out with hot water or saline, resulting in a dissolved or suspended hyperpolarized sample at room temperature. (E) In a clinical setting, the stable free radicals are filtered out. (F) The sample further undergoes a quality check to assure its compatibility with its intended use. (G and H) The sample is then injected into a subject, and an MRI scan is performed as soon as possible. The same procedure can also be used for *in vitro* experiments, skipping stages (E) and (F).

characteristic exponential decay time of the magnetization, denoted as T_1 , is not more than ~40 to 70 s (28). This is true even for pyruvate, which is the most favorable metabolite. That leaves only 2 to 3 min for the acquisition of useful spectroscopic image data after introducing the HP metabolite into the body. For other metabolites, such as glucose with $T_1 \sim 15$ to 20 s, the time window is much shorter. This short time window may be detrimental to the success of the measurement process because it must include the typical time of ~22 s from injection of the HP metabolite until it reaches the organ of interest (9), and also the time for said organ to metabolize the injected HP agent, which is ~15 s (9). Thus, during the time it takes for the probe to reach the organ of interest and become metabolized, the magnetization can decay altogether. Timing the MRI scan to occur within this temporal sweet spot is made even more difficult by the natural variability in different patients. Consequently, the measurement window is so narrow that it is often missed, which has detrimental implications on reliability, reproducibility, and utility of the method (9).

The severe problem of a short T_1 stems from the molecular nature of the metabolites in use. Increasing the magnetization lifetime requires manipulating their molecular size and environment. This cannot be done without changing their chemistry, thereby defeating the purpose of the experiment and its utility. A number of solutions to this problem have been proposed, such as the use of deuterated metabolites (29) and singlet state polarization storage (30). However, deuteration has proven insufficient to increase T_1 , reaching 20 s at most for glucose, for instance (31). Moreover, to the best of our knowledge, no relevant metabolite was found to be amenable for hyperpolarized biomolecular imaging applications using the singlet state approach (32). Consequently, the short T_1 problem is still a major unresolved issue.

Here, we report on a framework for providing highly polarized metabolites that retain their magnetization for many minutes, presumably also in *in vivo* circulation. This is achieved by cocrystallization of the

metabolite of interest with a matrix having a very long T_1 (in solid form), such as CaCO_3 . This matrix keeps replenishing the otherwise lost magnetization of the metabolite. As long as the cocrystallites are kept in solid form, magnetization is mostly preserved. Moreover, the method relies on the metabolite being released upon dissolution of the solute mainly near its target organ, triggered, for example, by pH levels. A possible scenario for the expected future use of our approach, as well as the experimental route we used here, is depicted in general terms in Fig. 2. In short, we build on our previous studies that drew inspiration from nature where intra-crystalline proteins were found to get incorporated into host CaCO_3 crystals (33–35). We further demonstrated that such an incorporation can be obtained also for single amino acids (36, 37) even in an incorporation level of up to 8% (38). We first describe the physical principles of our concept. Then, we provide experimental evidence to support our hypothesized magnetization retention mechanism. We further provide examples of hyperpolarized formulations effectively engineered to display this magnetization retention mechanism. Moreover, we demonstrate T_1 , hereafter denoted as T_1^\dagger , of more than 4 min for the metabolite inside the solid formulation in ambient conditions. This formulation is subsequently released into the solution, which then exhibits a liquid-state NMR signal with magnetization enhancement factors approaching four orders of magnitude. Our method addresses the major impediment that until now prevented the widespread use of HP metabolic MRI in routine clinical practice.

RESULTS

Concept and theoretical framework

Our approach for increasing the metabolites' T_1^\dagger is based on a concept we denote as matrix magnetization vehicles (MMV). The MMV approach (Fig. 3) uses a solid matrix exhibiting a particularly long T_1 as a polarization reservoir. If such a matrix is doped with any given metabolic molecular probe, then the polarization stored in it

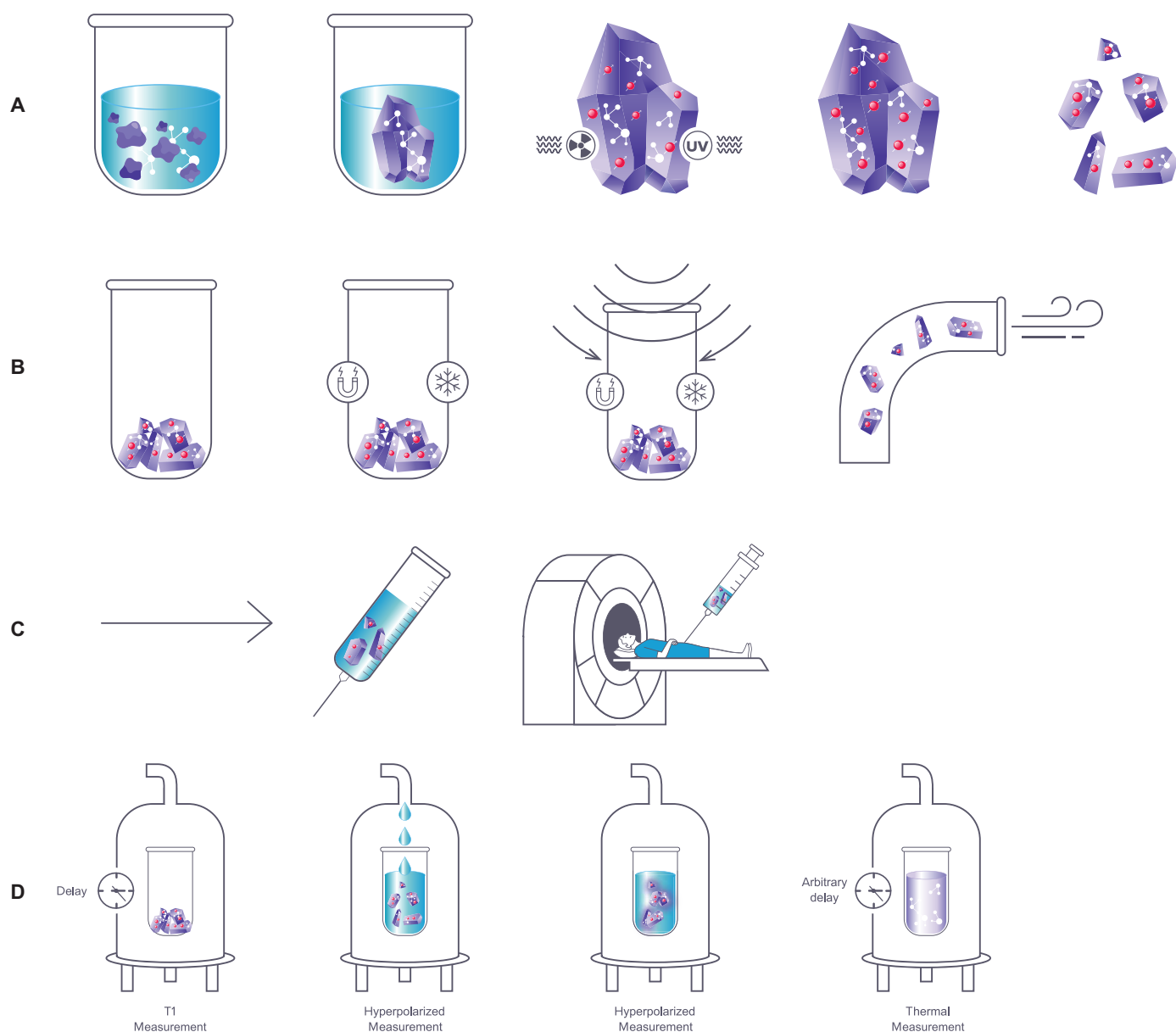


Fig. 2. The sample preparation procedure and proposed use case for our T_1 elongation concept. (A) Formulation preparation: A solution is prepared with both the metabolic probe (white molecule) and the polarization-preserving matrix (purple), followed by co-precipitation to form matrix crystals doped with metabolic probe molecules. Next, paramagnetic centers are formed in the doped crystals by way of γ -irradiation or UV irradiation. The crystals may then be micronized to an appropriate size for further use. (B) Bullet DNP polarization: The sample is placed inside a small bucket—the bullet—and subjected to low temperatures and a magnetic field. Under these conditions, it is MW-irradiated to induce electron-nuclei polarization transfer. Once an adequate level of nuclear polarization is reached, the sample is pneumatically shuttled out of the polarizer for further use. (C) Potential clinical application: Hyperpolarized formulation is added to saline to form a suspension and is subsequently administered to a patient. Dissolution occurs spontaneously inside the patient's body, preferably mostly in the organ of interest. (D) DNP experiment procedure used in this study: The pneumatically shuttled hyperpolarized sample is deposited inside an NMR spectrometer, and a T_1 measurement for the sample in its intact solid form is conducted. Next, a solvent is introduced, which dissolves the sample in situ in the spectrometer. The signal of the dissolved sample is measured while still hyperpolarized after having lingered in the spectrometer during the T_1 measurement. After an arbitrary delay, in which the hyperpolarized signal has decayed completely, a measurement of the thermal signal is acquired using multiple scans to assess the degree of HP.

can diffuse to the probe via spin diffusion, thereby replenishing polarization lost by the relatively fast T_1 relaxation mechanisms native to the probe molecule. This process keeps probe polarization well above its natural value, thereby effectively prolonging relaxation.

Polarization replenishment is governed by spin diffusion. The latter has been extensively studied in relation to NMR and to similar

two-level systems (39, 40). It can be approximately modeled as coherent transitions between states of a system subjected to dipolar interactions being turned on at some point in time (41). This model is helpful in predicting the behavior of spin diffusion as a function of various system parameters, although recent works suggest that spin diffusion is also composed of noncoherent processes (42). The

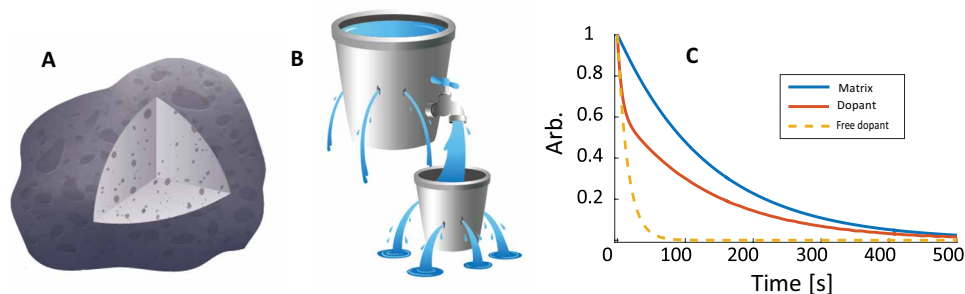


Fig. 3. The concept of MMVs. (A) Formulation used in this study. A crystalline matrix, characterized by a long T_1 , was doped with a metabolite of interest. Provided that both the metabolite and the matrix are composed of spin-half nuclei, then the spin lattice relaxation times of like spins in the two materials will probably approach each other. This results from spin diffusion taking place and transporting magnetization (without any physical movement) between the matrix nuclei and those of the dopant metabolite, and vice versa. The process is analogous to the coupled leaky buckets shown in (B). The large bucket with small leaks acts like the matrix spin bath, which can hold a large amount of magnetization and loses it slowly via relaxation processes associated with its relatively long T_1 . The small bucket plays the part of the smaller spin bath of the dopant, from which magnetization leaks substantially faster due to relaxation processes associated with a relatively short T_1 . The faucet replenishing the small bucket with water from the large bucket is analogous to spin diffusion transferring magnetization from the matrix spin bath to that of the dopant such that the magnetization of the dopant remains high as long as that of the matrix is high. (C) Results of a numerical simulation of magnetization decay in a matrix/dopant system experiencing interbath spin diffusion.

present research uses a phenomenological picture consisting of two spin baths experiencing relaxation and diffusion between them—a large bath with a long T_1 corresponding to the matrix, and a small bath with a short T_1 corresponding to the dopant metabolic molecule of interest. We conducted a numerical simulation (see section S3 for details) of the joint relaxation of two such coupled baths with the results shown in Fig. 3C. In this particular simulation, we considered the large matrix bath and the small dopant bath to display $T_{1\text{dopant}} = 30$ s, $T_{1\text{matrix}} = 300$ s, with an interbath coupling constant of $R = 10^{-5} \text{ s}^{-1}$ and a dopant matrix stoichiometric ratio of 1:50. In the absence of a polarization gradient, the two baths behave as if they are detached from one another. As a polarization gradient is formed, spin diffusion kicks in and the relaxation of the dopant bath is effectively slowed. The latter is seen as steep change in the time derivative of the dopant polarization graph at $t \sim 20$ s (Fig. 3C). We now demonstrate and experimentally test the spin diffusion mechanism in several dopant-matrix systems that are relevant to metabolic MRI.

Measuring the increase in T_1^\dagger of dopant molecule

We first show and explore the phenomenon of increase in T_1^\dagger of the dopant molecule. Experiments were conducted on a sample of aspartic acid in CaCO_3 , termed Asp1 (see Materials and Methods and the Supplementary Materials for sample details and preparation protocol), in which all carbons (i.e., both in the inorganic matrix and in the organic dopant) were labeled with the NMR active ^{13}C isotope. Sample Asp2 was used as a control, prepared with ^{13}C -labeled organic dopant but without labeling the matrix carbons. Measurements of both samples were conducted at room temperature, field of 300 MHz, and magic angle spinning (MAS) frequency of 10 kHz. Sample Asp1 has a magnetization reservoir in the form of matrix ^{13}C spins, but Asp2 lacks it. This is because the amount of ^{13}C spins in the matrix of Asp2 is two orders of magnitude lower (i.e., only $\sim 1\%$ natural abundance was available) and also because the scarcity of the ^{13}C nuclei greatly diminished (although not completely eliminated) the efficiency of spin diffusion.

First, a direct assessment of the relaxation rates for sample Asp1 and a rougher assessment for sample Asp2 (owing to the notoriously

long nature of such measurement) were made using the saturation recovery technique. Saturation recovery employs a standard echo experiment at varying shot repetition time delays (fig. S6). The results of these experiments are shown in Fig. 4. The matrix value of T_1 in sample Asp1 was deduced by exponential fitting, which provided a T_1 value of over 6 min. The partial sampling of the relaxation process in sample Asp2 mandated a customized estimation of T_1 and T_1^\dagger (see the Supplementary Materials for details). As shown in Fig. 4, labeling the matrix with ^{13}C leads to an almost 10-fold elongation of T_1^\dagger the dopant metabolite.

To demonstrate the generalizability of this technique, another formulation of calcium carbonate was tested using glycine instead of aspartic acid as a dopant. These tests were conducted at room temperature, field of 200 MHz, and MAS frequency of 5 kHz. Again, we used a formulation in which both the glycine and the carbonate matrix were ^{13}C -enriched (Gly1) and a control formulation in which only the glycine carbons were ^{13}C -enriched (Gly2). The results (Fig. 5) show that T_1^\dagger for the amino acid in sample Gly1 exceeds T_1^\dagger in sample Gly2 by two orders of magnitude, confirming that spin diffusion-mediated T_1^\dagger elongation is at play.

Spin diffusion mechanism—metabolite to matrix

To better explain our T_1^\dagger elongation observation, we further investigated the spin diffusion mechanisms in our sample. The tests in this section were conducted at room temperature, field of 300 MHz, and MAS frequency of 10 kHz. We used cross polarization (CP), which allows the transfer of magnetization from hydrogen nuclei to ^{13}C nuclei (and, more generally, between any two baths of different spins) (43, 44). This technique only works between nuclei situated in very close proximity, such as those directly bonded to one another, or with those that are two to three bonds apart at most (43, 44). Hence, one can selectively address carbons that are in sufficiently close proximity to hydrogen atoms (such as all carbons belonging to aspartic acid or glycine in our samples) while leaving all others unaffected. Furthermore, the sense of the transferred polarization can be controlled (either parallel or antiparallel to the static magnetic field) (44), permitting cancelation of noninverting disturbances—an attribute we will be

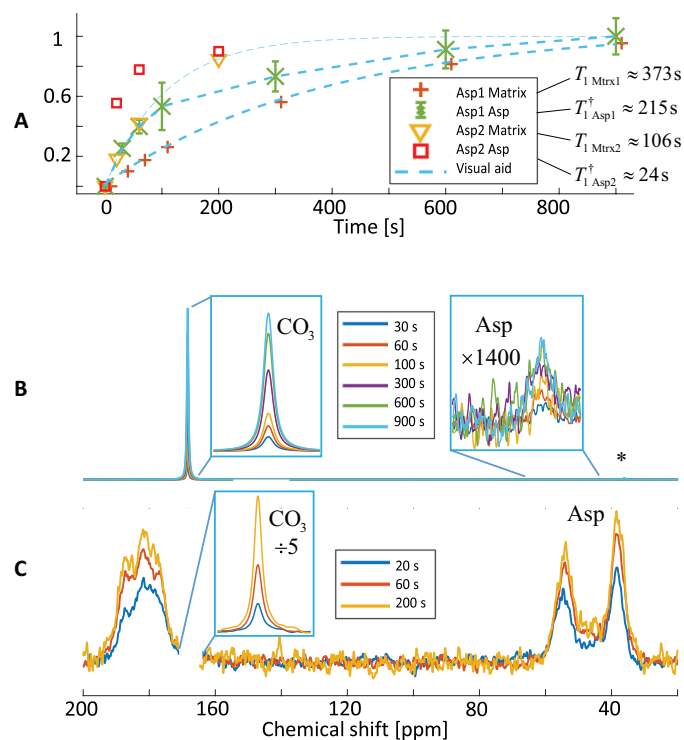


Fig. 4. Direct measurement of ^{13}C T_1 relaxation for samples Asp1 and Asp2. (A) Integrals of the main spectral peaks for samples Asp1 and Asp2 for different shot repetition delays (buildup time). (B) Spectra taken for sample Asp1, from which the graphs in (A) are derived. (C) Same as (B) but for sample Asp2, in which the carbonate matrix is not labeled. The assignment of the peaks in the spectra is as follows: acid carboxyls: 182 ppm; matrix carbonate: 168.4 ppm; acid α carbon: 54 ppm; and acid β carbon: 39 ppm. (B) shows only the peaks that can be viewed free from interferences of wide-band features and spinning sidebands.

using in our spin diffusion measurement procedure. In addition, CP can be used to drain polarization from carbons in close proximity to hydrogens. This important property will also be used in this work. The specific CP sequences used in this work are shown in figs. S7 to S9.

We first show how magnetization diffuses from the aspartic acid dopant to the surrounding matrix in sample Asp1, using the first type of spin diffusion pulse sequence (fig. S7). This is demonstrated by selectively polarizing carbons via CP, which only affects aspartic acid carbons (i.e., those that are attached to hydrogen) and also a small portion of matrix carbons that reside close to hydrogen atoms (see fig. S1). The vast majority of matrix carbons are unaffected by this process. All spin diffusion experiments use phase cycling that eliminates background thermal polarization and leaves intact only polarization that originates from the CP process. As the magnetization at various delays after the application of CP is sampled, magnetization diffusion from the aspartic acid ^{13}C spins to the matrix carbonates in the spin bath is observed (Fig. 6A). These data demonstrate that over a few seconds, magnetization in the sample is conserved and only flows from one spin bath (that of the aspartic acid) to another (that of the matrix), as illustrated in Fig. 6C. Conducting the same experiment for sample Asp2 results in completely different outcomes because the carbonate spin bath does not sustain long-range spin diffusion (Fig. 6B). These results demonstrate that in the case of Asp2, the magnetization imparted to the aspartic acid ^{13}C nuclei has

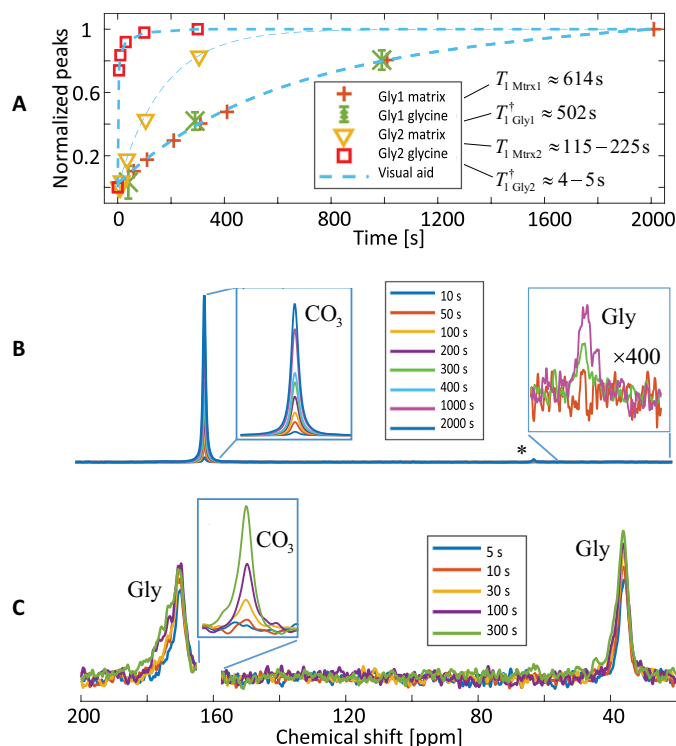


Fig. 5. Measurement of T_1 relaxation for samples Gly1 and Gly2. (A) Integrals of the relevant spectral peaks for samples Gly1 and Gly2. (B) Spectra taken for sample Gly1, from which the graphs in (A) are derived. (C) Same as (B) but for sample Gly2, for which the carbonate matrix was not labeled. The assignment of the peaks in the spectra panels (B) and (C) is as follows: acid carboxyl: 171 ppm; matrix carbonate: 161.4 ppm; and acid α carbon: 36 ppm. (B) does not show the acid carboxyl peak that is obscured by the wide-band feature of the matrix carbonate.

nowhere to diffuse, while the polarized aspartic acid carbons of sample Asp1 can rapidly drain their polarization into the surrounding enriched matrix (Fig. 6D). Therefore, the aspartic acid's polarization in sample Asp2 remains locked in place and decays owing only to its T_1 .

The above experiments were all conducted with a spinning frequency of 10 kHz. Running the same experiments also at spinning frequencies of 14 and 8 kHz reveals how spin diffusion correlates inversely to this frequency [see fig. S11 and related text in the Supplementary Materials (45)]. This explicit illustration of how spinning-induced suppression of the dipolar interaction degrades spin diffusion highlights the fact that spin diffusion is mediated by dipolar interactions. The fact that MAS suppresses dipolar interactions, and thus suppresses dipolar interaction-mediated spin diffusion, constitutes the reason we chose to run our experiments with Gly1 and Gly2 samples, as well as our matrix to metabolite spin diffusion experiments (see the next section), at relatively low spinning frequencies of 5 kHz.

Spin diffusion mechanism—matrix to metabolite

We next evaluate the phenomenon of polarization diffusion from the matrix to the dopant molecule (aspartic acid in our case), which gives rise to the effective T_1^\dagger elongation. A polarization gradient between the two baths is necessary for prompting spin diffusion in the desired direction. Therefore, to observe this mechanism in the

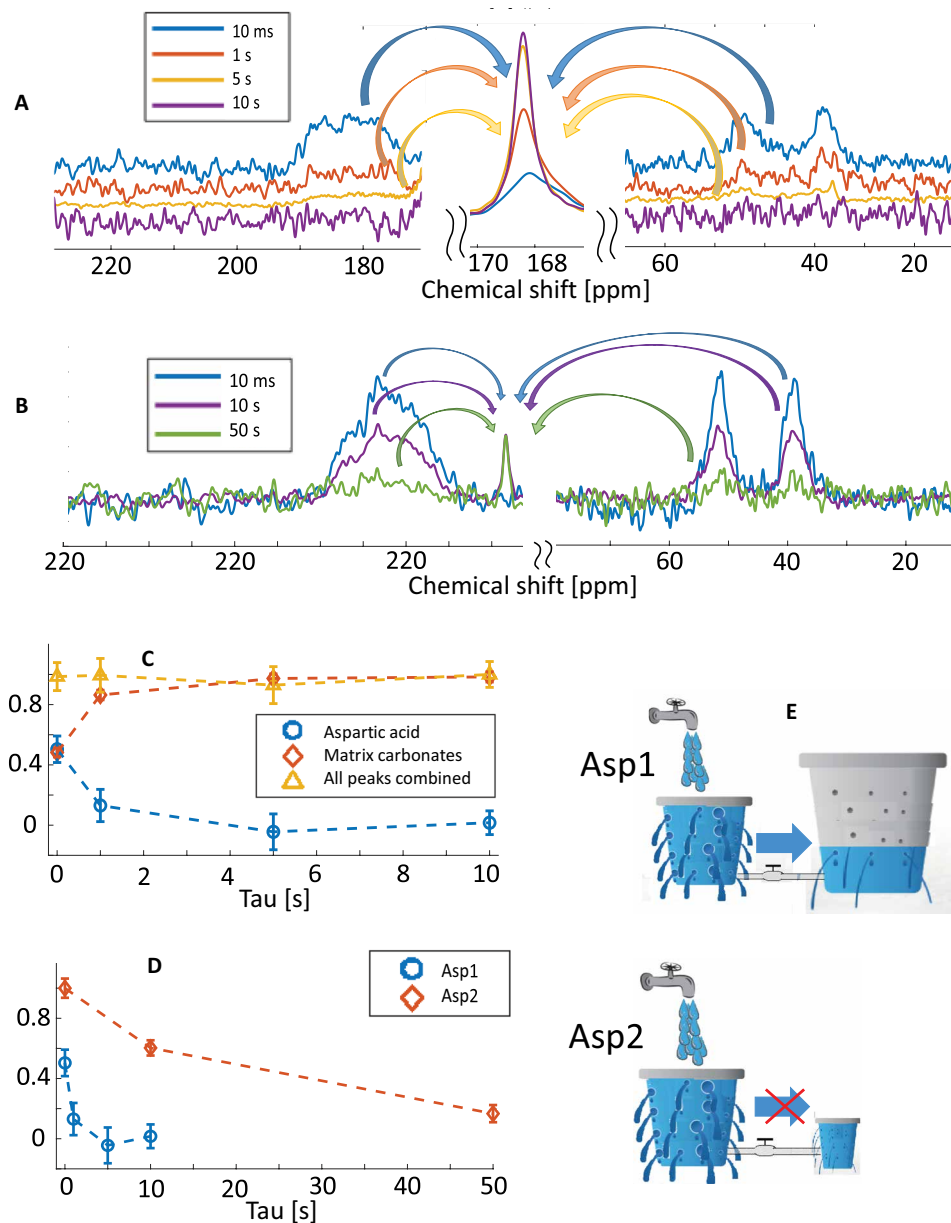


Fig. 6. ^{13}C spin diffusion in samples Asp1 and Asp2 with an illustration of the process using bucket diagrams. (A) Spectra of Asp1, acquired at various delays following CP polarization of the near-hydrogen carbons, illustrating the flow of polarization from the falling broad aspartic acid peaks (found around 39, 54, and 182 ppm) to the rising narrow carbonate peak (at ~ 168 ppm). (B) Data from a similar set of experiments conducted for sample Asp2, which demonstrate the impaired flow of polarization between spin baths. (C) Plots derived from the data of Asp1 show the evolution of the integrals of the aspartic acid peaks, the carbonate matrix peak, and their sum. (Dashed lines are a visual aid to help the reader appreciate the trend.) (D) Comparison between the evolutions of the aspartic acid peaks of samples Asp1 and Asp2. It shows that the drainage of polarization to the matrix in Asp1 is almost instantaneous, while for Asp2 the decay is governed by what seems to be normal thermal relaxation. (E) Illustration of how a filled small bucket, representing the polarized aspartic acid carbons following the CP polarization process, can drain quickly into a large empty bucket, which is analogous to the enriched matrix. It further shows how this process is blocked, to a great extent, if the receiving bucket is tiny and suffers from less effective transfer, a situation akin to that of the nonlabeled matrix of sample Asp2.

present set of experiments, the matrix and aspartic acid spin baths should be maximally and minimally polarized, respectively. To avoid exceedingly long experiments associated with the slow relaxation of the matrix, CP and spin diffusion are used to speed up the attainment of matrix polarization by way of our CP pump pulse sequence (fig. S8). With this sequence, aspartic acid ^{13}C spins are

polarized via CP from the acid protons. This process can be repeated rapidly as it is only limited by the very rapid relaxation of the hydrogen nuclei that act as the polarization source. Polarization then diffuses from the aspartic acid to the matrix. The process is repeated multiple times until the matrix polarization approaches that of a freshly polarized bath of aspartic acid spins. This process is

referred to as the CP pump (fig. S8). The buildup of matrix polarization as a function of the number of pump cycles is presented in fig. S10.

Once the matrix carbons are maximally polarized, the next step is to create a polarization gradient between the matrix and the aspartic acid. This allows us to observe polarization diffusing back to the aspartic acid via the reverse spin diffusion pulse sequence (fig. S9). CP depolarization is used to facilitate the required polarization gradient by transferring ^{13}C spin polarization of the aspartic acid to a depolarized bath of its hydrogen spins. Spin diffusion then occurs from the polarized matrix to the depolarized aspartic acid ^{13}C spins. Figure 7A shows the behavior of one of the aspartic acid peaks following this double CP process. The inset above the main panel shows the integral of that peak for improved clarity. Immediately after polarization drainage to the aspartic acid proton bath, the peak is weak but still visible. As time is allowed for spin diffusion to proceed, the peak reemerges. The process is so effective that the peak of the aspartic acid is still present even after 200 s. (Note that the thermal signal is canceled by phase cycling; refer to section S2.2.) The survival of aspartic acid polarization for such a long duration can only be attributed to the spin diffusion-based mechanism inducing an effective relaxation elongation. Conversely, when conducting the same experiment for sample Asp2 (Fig. 7B), no resurgence of the peak is observed. The inset depicts the integral of the portrayed peak of Asp2. A clear and uninterrupted decay of polarization is observed, as is expected from any ordinary sample undergoing T_1 relaxation. After 200 s, the peaks of the aspartic acid have decayed completely.

DNP experiments

As a concluding step, we demonstrate the viability of our methodology in HP experiments. To make the samples amenable to DNP, one must first dope them with paramagnetic species. This process may alter some of the sample's characteristics. Therefore, the DNP experiments should clarify the following three critical questions: (i) Can these solid samples be polarized effectively? (ii) What is the effect of paramagnetic dopants in the solid sample (required for the DNP process) on its T_1 and on T_1^\dagger of the dopant? (iii) Does the T_1^\dagger elongation mechanism, demonstrated to work at normal thermal polarization conditions, perform as effectively when the sample is hyperpolarized?

The DNP experiments were conducted with two types of samples: The first one is the Gly1 described above, and the second one is GlucPyr, consisting of ^{13}C -labeled fully deuterated glucose doped with $2\text{-}^{13}\text{C}$ pyruvic acid (see section S1.3 for details). The latter sample was chosen with the expectation that the same spin diffusion-based T_1^\dagger elongation mechanism would make use of the long T_1 of the solid glucose to prolong the T_1^\dagger of the pyruvic acid. In its native form, pyruvic acid is a liquid at room temperature and thus is not expected to sustain any kind of spin diffusion. However, if it is enveloped sufficiently tightly in the host solid, it may be immobilized to a degree that can allow spin diffusion to proceed.

Unpaired electrons were imparted to sample Gly1 by γ -irradiation (46) and to sample GlucPyr by ultraviolet (UV) irradiation (47) (see sections S1.2 and S1.3 for full details). Thus, in both samples, the unpaired electrons that are required for DNP were intrinsic. For sample Gly1, particle size was assessed using scanning electron microscopy images and found to be in the range of 10 to 20 μm (see

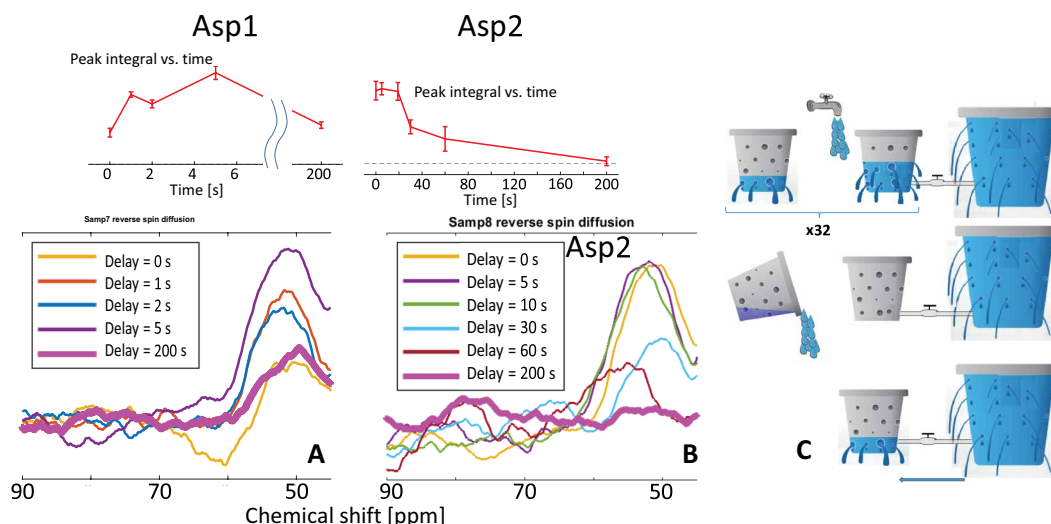


Fig. 7. ^{13}C spin diffusion from matrix to metabolite. (A) One of the aspartic acid peaks for sample Asp1, as observed after various delays in which spin diffusion was allowed to proceed from a maximally polarized matrix back to the polarization-depleted aspartic acid carbons (see also fig. S9). This peak was chosen because it is free from interferences of spinning sidebands from the intense matrix peak. One may clearly appreciate the resurgence of the peak as spin diffusion is allowed to proceed. (B) Results of an identical experiment performed on sample Asp2, in which the matrix cannot serve as a polarization reservoir due to the absence of ^{13}C enrichment. The peak at a delay of 0 is suppressed by CP, but not completely. As the delay increases, the peak simply decays due mainly to T_1 relaxation, which is barely affected by spin diffusion from the matrix (i.e., the few natural abundance carbon spins cannot serve as an effective polarization reservoir in this sample). In this case, observation after 200 s shows that the peaks have completely decayed. The time-dependent integrals of the Asp1 and Asp2 peaks are shown, respectively, on top of (A) and (B). (C) Pictorial illustration of the various stages of the experiment for the Asp1 sample: First, the matrix is polarized using the CP pump scheme described above, illustrated by the filling of the large bucket at the top of the panel. Next, the water in the small bucket is dumped; this is analogous to the CP-mediated depolarization of the aspartic acid carbons. This creates a polarization gradient between the aspartic acid and the matrix carbons that prompts spin diffusion to occur, illustrated by the water flowing back from the large full bucket to the small empty one at the bottom of the panel.

the Supplementary Materials for details). For sample GlucPyr, no such assessment was needed as particle/conglomerate size was in the range of hundreds of micrometers as could be seen by eye. Although the current size distribution is not compatible with *in vivo* application, we have conducted measurements that show that reducing the size to less than 1 μm does not degrade T_1 considerably in these systems (see section S1.4).

The experiments for both samples were conducted according to the following procedure (see also Fig. 2): The samples were inserted into the polarizer, where they underwent the DNP process for about 17 hours (see fig. S12 for buildup curves). Following this, the samples were pneumatically shuttled through a magnetic tunnel into an NMR tube already in place inside an adjacent NMR magnet. The solid-state NMR signal was then acquired using a tip angle of 10° and pulse delays of 30 and 20 s (for Gly1 and GlucPyr, respectively). Signal acquisition started automatically upon sample arrival at the spectrometer.

The data thus gathered are shown in Fig. 8. It suffers from some receiver saturation effects but still enables us to estimate the T_1 values of our samples, found to be about 232 s for Gly1. It should be noted that T_1 values of 9 and 21 min were found in experiments dedicated to measuring T_1 of hyperpolarized Gly1 in its solid form at ambient conditions that lacked the dissolution stage and therefore could persist for much long time beyond the stage where receiver saturation presents a problem (see fig. S13). For the GlucPyr sample, a more complicated behavior is found in the solid state at ambient conditions (Fig. 8B). The spectrum acquired immediately upon sample arrival ($t = 0$ in Fig. 8B) reveals clear spectral features of a liquid compartment. The scan gathered 20 s later shows that the peaks coming from the liquid compartment have decayed completely. Only a broad line remains, which displays a T_1 of ~ 410 s. Judging by the symmetric Gaussian line shape seen in Fig. 7B, this line originates from an amorphous compartment. There is no trace of pyruvic acid signal in the post-dissolution hyperpolarized

spectra. Therefore, it seems that the pyruvic acid and the glucose matrix failed to mix at the molecular level. One possible explanation is that the sample is composed of large domains of crystalline glucose surrounded by a layer whose outer part is composed of a very mobile/liquid phase of glucose/pyruvic acid solution, and whose inner part is largely composed of amorphous glucose. This picture receives further support from retrospective MAS-NMR carried out for the same sample (see section S15). The liquid compartment is polarized by the UV-generated pyruvic acid radicals. This polarization also seeps into the amorphous glucose layer by spin diffusion but fails to penetrate further into the bulk crystalline compartment. Since pyruvic acid is only present in the liquid compartment, its polarization is not replenished by our spin diffusion mechanism and thus it does not survive even 1 min in ambient conditions and decays before dissolution.

Following the solid-state measurements, about 150 and 60 s after sample arrival, for Gly1 and GlucPyr, respectively, a second acquisition was initiated, with scans being taken 1 s apart and using a tip angle of 10° . Shortly after this scan initiation, an aqueous medium was introduced into the tube (5% HCl in D_2O and neat D_2O , for Gly1 and GlucPyr, respectively) to dissolve the sample. The solution that formed contained the hyperpolarized probes at concentrations of the order of 50, 20, and 190 mM for glycine, pyruvic acid, and glucose, respectively. The introduction of the liquid was accompanied by turbulences in the content of the tube, which dissipated within a few seconds. Therefore, we present the data of the earliest scan not affected by it in Fig. 9 (see fig. S14 for complementary liquid-state data). At the end of the hyperpolarized liquid measurement, and after complete decay of the hyperpolarized magnetization, measurement of the thermal signal was performed. For sample Gly1 in its dissolved form, the thermal signal measurement used 3189 acquisitions, with 20-s pulse delay and 10° tip angle. For GlucPyr, 2181 acquisitions were recorded with 5-s repetition delay and 30° tip angle. The hyperpolarized liquid NMR spectra are compared to their

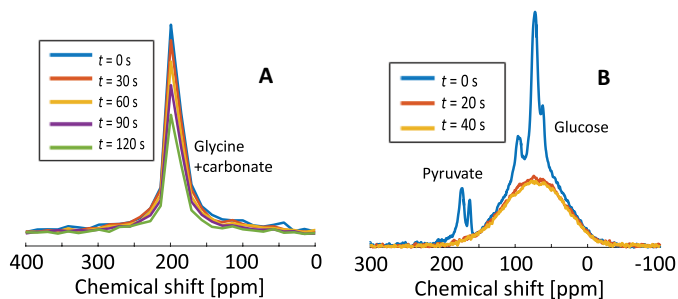


Fig. 8. HP experiments for samples Gly1 and GlucPyr. (A) Signals acquired for sample Gly1 in the spectrometer immediately after bullet shuttling of the sample from the polarizer to the spectrometer. The legend depicts the time points at which spectra were taken using a small tip angle. We note that in the derivation of these peaks, the initial sections of the time domain data are cut off on account of the receiver being saturated at the beginning of the free induction decay, owing to the intensity of the NMR signal. (B) Spectra of the post-shot acquisitions, with legend depicting the time points at which spectra were taken using a small tip angle. In the first spectrum (at $t = 0$), the familiar liquid-state spectral contour of glucose is clearly visible, as is that of pyruvic acid at ~ 170 ppm. The liquid-state component decays completely during the 20-s delay until the next acquisition. After 20 s in ambient conditions, only the solid-state component persists. Only the last two traces are used to assess T_1 in the solid state for this sample.

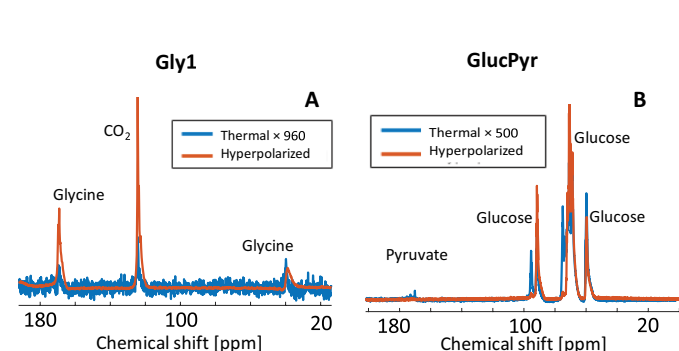


Fig. 9. Hyperpolarized spectra shortly after dissolution versus thermal spectra. The data demonstrate the preservation of HP in ambient conditions and the enhancement factors that remain available in the liquid state after a considerable time interval. The respective spectra come from the same samples used to produce the data in Fig. 8. (A) Liquid-state signal of hyperpolarized glycine superimposed with the thermal signal representing a magnetization enhancement factor of $\epsilon \approx 2200$ for the aliphatic peak and $\epsilon \approx 10,200$ for the carboxyl peak preserved by virtue of the spin diffusion mechanism. (B) Liquid-state signal of hyperpolarized glucose as acquired shortly after dissolution, superimposed with the thermal signal, representing an enhancement of ~ 870 at the time of dissolution preserved over more than 60 s in ambient conditions by virtue of residing in the solid state.

thermal counterparts to estimate the signal enhancement. For the Gly1 sample, we find enhancement factors of $\epsilon \approx 2200$, and 10,200 (corresponding to absolute polarization of $P_N = 1.8\%$, $P_N = 8.2\%$), for the α and carboxyl carbons, respectively (at an applied magnetic field of 400 MHz). This finding confirms that T_1^\dagger elongation took place in the hyperpolarized Gly1 sample, for the magnetization of the hyperpolarized glycine could not have survived otherwise.

Regarding the GlucPyr sample, the spectrum after dissolution does not display the pyruvic acid peak since its hyperpolarized signal already decayed during the prolonged period of the solid-state NMR signal acquisition, as described above (Fig. 8B). Nevertheless, the glucose spectrum does display a noticeable hyperpolarized signal, reflecting an enhancement of $\epsilon \approx 870$ ($P_N = 0.7\%$) with respect to its thermal counterpart (Fig. 9B). (Refer to sections S9 and S12 to S14 for a detailed account of the derivations of T_1 values and enhancement factors.)

DISCUSSION

A mechanism for maintaining hyperpolarized NMR signal of common metabolites (prepared in a unique matrix formulation) for an extended period of time was demonstrated by experiments and explained both theoretically and methodically. The polarization retention mechanism is sufficiently effective to allow exceedingly long T_1 values for the intact formulations in ambient conditions even in the presence of free radicals, reaching values of 410 and 230 s for GlucPyr and Gly1 formulations, respectively. Furthermore, T_1^\dagger for the glycine molecule residing in the Gly1 formulation is similar to the T_1 value of the formulation as a whole (based on its high liquid-state polarization and on our NMR-MAS observations). The level of absolute polarization that we reached (more than 8% in some samples) is close to those being used today in man. The latter usually use a metabolic agent at a nuclear polarization of $>15\%$ (21, 25). These findings alone represent an improvement of >3 -fold in the usable magnetization lifetime, compared to the gold standard of HP pyruvate [$T_1 \sim 67$ s—usable magnetization lifetime of ~ 3 min (28)]. Namely, we expect a usable magnetization lifetime of about 10 min. Moreover, in other experiments dedicated to the elucidation of the T_1 of sample Gly1 in its intact solid form, T_1 values as high as 21 min were observed. The approach we take is of a rather general nature and could be applied also to other metabolites that may have much lower intrinsic T_1 and also for other matrixes. The implications of these findings are far-reaching. Not only are long-lived viable hyperpolarized metabolites created but also the procedures for polarizing them are mostly compatible with existing commercially available polarizers, such as Hypersense (by Oxford Instruments) and possibly even Spinlab (by GE Medical) systems. All of these systems have DNP procedures not requiring advanced dual microwave/radio frequency capabilities beyond mere monitoring of the polarization buildup. Additionally, the polarizing agents we use are composed of nonpersistent radicals. Because these species self-annihilate, they do not require cumbersome removal during the precious lifetime of the hyperpolarized magnetization (47, 48).

It is important to consider the biocompatibility and pharmacokinetic properties of our formulations, the expected concentration of the hyperpolarized metabolites in the organ of interest, and the time in which the organs can be reached. Whole-body concentrations used in metabolic MRI in man are typically about ~ 0.23 mM (4). We now discuss the safety and feasibility of our approach in man.

Biocompatibility

The toxicity associated with the sudden administration of large quantities of calcium may pose a serious concern, as elevation of serum calcium levels from the normal range of 90 to 105 mg/liter to above 150 mg/liter may be fatal (49). To address this concern, we first state that it is a standard practice to administer dissolved calcium at rates of 0.7 mmol/min with total doses of 6.7 mmol and beyond (50). Considering the slow dissolution rate of calcium carbonate at normal physiological conditions, which may even span days (51), a dissolution rate of 0.7 mmol/min would be the result of the administration of ~ 100 g of calcium carbonate agent, which is an order of magnitude higher than we deem necessary (please see below). Also, in view of the fact that calcium carbonate nanoparticles have been successfully and safely previously used in *in vivo* research (52–54), it follows that the transient release of free calcium into the blood does not constitute a limiting factor. A further concern may be the particulate nature of our formulation; however, animal experiments have shown that ~ 1 - μm particles at a total particle volume with doses well over 32 $\mu\text{l}/\text{kg}$ are safe (55). For calcium carbonate-based formulations, this translates to ~ 0.1 g/kg. For a metabolic probe at stoichiometric content of $\sim 5\%$, such as that of Gly1 (37, 56), this dose translates to a whole-body concentration of ~ 5 mM—well above the value of 0.23 mM, commonly used as the whole-body concentration of a hyperpolarized metabolic probe in recent preclinical work on metabolic MRI in humans (4). Given the above considerations, the dose limiting factor is the particulate nature of the agent. A permissible dose of ~ 0.1 g/kg of calcium carbonate-based agent far exceeds the familiar 0.23 mM of hyperpolarized agent used in recent works. Clearly, the particle size of sample Gly1 is too large for intravenous administration, and reducing it may jeopardize the T_1 properties of the material. However, past experience with similar samples shows that reducing the size to around 1 μm is not expected to have a strong effect (see section S1.4).

Pharmacokinetics

Section S16 provides a brief analysis for estimating the rate of release of a hyperpolarized metabolic probe embedded in calcium carbonate particles at an inclusion level of $\sim 5\%$, similar to Gly1. Using fundamental acid/base chemistry principles, it can be shown that at the decreased pH (about 6.5) associated with tumor environments (57), combined with natural bicarbonate buffering system (58) and respiratory equilibration mechanisms (59) at play in mammalian physiology, a local release of the hyperpolarized metabolic probe at a rate of ~ 0.02 mM/min (54) is possible (60) (see section S16). This release may lead to accumulation of 0.1 mM of hyperpolarized probe over a period of ~ 5 min, which is well within the time window allowed by the T_1^\dagger values demonstrated in this work. This value is on par with the order of magnitude of ~ 0.23 mM currently in used in human metabolic MRI preclinical work. Future formulations may trigger faster release in the organ of interest. In general, the local manner in which the agent dissolves hold two benefits. (i) The amounts of free calcium released in the body are small and do not pose danger, and (ii) the small total amount of agent that ultimately dissolves ensures that the overall amount of intact circulating particles is kept relatively constant within the relevant time window of a few minutes and that the site of interest is constantly resupplied with more agent particles conveyed by the bloodstream.

While our proposed approach is very promising, it also has some limitations and drawbacks, and the road to clinical use in humans is still long. The process of preparing the amalgamized samples is not

Table 1. List of samples used in our experiments.

Sample	Matrix	Dopant	Measurement
Asp1	Ca ¹³ CO ₃	Aspartic acid, 4- ¹³ C, 1- ¹⁵ N	NMR
Asp2	CaCO ₃	Aspartic acid, 4- ¹³ C, 1- ¹⁵ N	NMR
Gly1	Ca ¹³ CO ₃	Glycine 2- ¹³ C, 1- ¹⁵ N 2- ¹³ C	NMR DNP
Gly2	CaCO ₃	Glycine 2- ¹³ C, 1- ¹⁵ N	NMR
GlycPyr	Glucose 6- ¹³ C, 12- ² H	Pyruvic acid, 1- ¹³ C	DNP

trivial, and it is not clear yet if this cocrystallization approach can work for all metabolites of interest. The metabolites are diluted during the cocrystallization process by a typical factor of ~25 to 100, compared to the pure solid material. More work is required to confirm the safe injection of the solid cocrystallites into the body and to improve the trigger of their dissolution in specific organs of interest. For CaCO₃ cocrystallites, which are not soluble at normal blood pH levels but dissolve in low pH, one can envision a targeted dissolution in cancerous tissues that exhibit high enough acidity. Overall, we believe that this approach represents an important advance toward the widespread clinical adoption of hyperpolarized metabolic MRI probes with much less time limitation, thereby enabling metabolites of interest to reach organs throughout the body and image their metabolic activity noninvasively.

MATERIALS AND METHODS

Materials

All labeled materials used in this study were enriched to ~100% with their respective isotopes. Labeled materials were obtained from Cambridge Isotope Laboratories and Cortecnet. Sample Asp1 (Asp2) was prepared at room temperature by slow precipitation of ¹³C-labeled (nonlabeled for Asp2) calcium carbonate from an aqueous solution by dripping 1.5 ml/min of 50 mM CaCl₂ solution into 50 mM Na₂CO₃ solution, both containing ¹³C- and ¹⁵N-labeled aspartic acid at a concentration of 2.6 mM (see the Supplementary Materials for details). The stoichiometric content of aspartic acid was measured by elemental analysis to be 0.45% (0.53%). Sample Gly1 (Gly2) was prepared at room temperature by flash precipitation of ¹³C-labeled (nonlabeled for Gly2) calcium carbonate from 0.2 M aqueous solutions of Na₂CO₃ and CaCl₂ with the previous also containing 0.2 M of ¹³C- and ¹⁵N-labeled glycine, followed by incubation in an autoclave for ~2 hours at 134°C (37, 56). (In the case of sample Gly1 used in the DNP experiments, glycine was labeled only with ¹³C and not with ¹⁵N.) The stoichiometric content of glycine in the samples was not directly measured but is expected to be ~5% (37, 56). All calcium carbonate-based samples were centrifuged and thoroughly rinsed and dried after synthesis.

Before further study, the synthesized crystals were characterized via high-resolution synchrotron powder diffraction at ID22 (61) of the European Synchrotron Radiation Facility (Grenoble, France). When incorporation of an amino acid is achieved, the diffraction peaks of the calcite host crystals are shifted to lower degrees, which corresponds to an increase in the d-spacings. An example of such a shifted diffraction peak is shown in fig. S1.

Sample GlucPyr was prepared by slow crystallization from a concentrated aqueous (heavy water) syrup of ¹³C/²H-labeled glucose in the presence of pyruvic acid labeled with ¹³C at the carboxyl position. Samples destined for DNP experiments had to be imparted with paramagnetic centers that serve as polarizing agents. To that end, sample Gly1 was γ -irradiated at room temperature for ~4 hours using a ⁶⁰Co source (photon energies of 1.33 and 1.17 MeV), culminating at a nominal dose of 30,000 Gy (46), and resulting in a radical content of the order of 10 mM. For sample GlucPyr, this was accomplished by UV irradiation under liquid nitrogen (47) shortly before the experiment commenced, resulting in an overall radical concentration of the order of 10 mM, which is very likely to be distributed nonhomogeneously within the sample.

An additional characterization, applied only to sample Gly1 from the DNP batch, was evaluated in a scanning electron microscope, demonstrating that the sample was composed of particles with crystalline geometry and a diameter of roughly 20 μ m (see the Supplementary Materials).

For detailed descriptions of the preparation protocols of each sample used here, refer to the Supplementary Materials. A summary of sample details is given in Table 1.

NMR and DNP systems

Experiments on samples containing aspartic acid and glycine were conducted on Bruker Avance III systems operating at 300 and 200 MHz, respectively, at ambient conditions. DNP experiments were conducted on a homebuilt “bullet DNP” polarizer operating at 6.7 T in conjunction with a Bruker Avance II NMR spectrometer operating at 400 MHz. A detailed description of the apparatus was previously published (62, 63). The NMR and DNP pulse sequences used in this work are detailed in the Supplementary Materials.

Supplementary Materials

This PDF file includes:

Sections S1 to S16
Figs. S1 to S15
References

REFERENCES AND NOTES

1. A. Adam, A. K. Dixon, J. H. Gillard, C. Schaefer-Prokop, *Grainger & Allison's Diagnostic Radiology* (Elsevier, 2020).
2. T. S. Curry, J. E. Dowdey, R. C. Murry, *Christensen's Physics of Diagnostic Radiology* (Lippincott Williams & Wilkins, 1990).
3. R. Woitek, F. A. Gallagher, The use of hyperpolarised ¹³C-MRI in clinical body imaging to probe cancer metabolism. *Br. J. Cancer* **124**, 1187–1198 (2021).

4. N. Sushentsev, M. A. McLean, A. Y. Warren, A. J. V. Benjamin, C. Brodie, A. Frary, A. B. Gill, J. Jones, J. D. Kaggie, B. W. Lamb, M. J. Locke, J. L. Miller, I. G. Mills, A. N. Priest, F. J. L. Robb, N. Shah, R. F. Schulte, M. J. Graves, V. J. Gnanapragasam, K. M. Brindle, T. Barrett, F. A. Gallagher, Hyperpolarised (13)C-MRI identifies the emergence of a glycolytic cell population within intermediate-risk human prostate cancer. *Nat. Commun.* **13**, 466 (2022).
5. S. Anderson, J. T. Grist, A. Lewis, D. J. Tyler, Hyperpolarized (13) C magnetic resonance imaging for noninvasive assessment of tissue inflammation. *NMR Biomed.* **34**, e4460 (2021).
6. C. Najac, M. M. Chaumeil, G. Kohanbush, C. Guglielmetti, J. W. Gordon, H. Okada, S. M. Ronen, Detection of inflammatory cell function using 13C magnetic resonance spectroscopy of hyperpolarized [6-13C]-arginine. *Sci. Rep.* **6**, 31397 (2016).
7. J. J. Miller, A. Z. Lau, P. M. Nielsen, G. McMullen-Klein, A. J. Lewis, N. R. Jespersen, V. Ball, F. A. Gallagher, C. A. Carr, C. Laustsen, H. E. Bøtker, D. J. Tyler, M. A. Schroeder, Hyperpolarized [1,4-(13)C(2)]fumarate enables magnetic resonance-based imaging of myocardial necrosis. *JACC Cardiovasc. Imaging* **11**, 1594–1606 (2018).
8. T. R. Carver, C. P. Slichter, Experimental verification of the Overhauser nuclear polarization effect. *Phys. Rev.* **102**, 975–980 (1956).
9. M. Vaeggemose, R. F. Schute, C. Laustsen, Comprehensive literature review of hyperpolarized carbon-13 MRI: The road to clinical application. *Metabolites* **11**, 219 (2021).
10. J. H. Ardenkjaer-Larsen, B. Fridlund, A. Gram, G. Hansson, L. Hansson, M. H. Lerche, R. Servin, M. Thaning, K. Golman, Increase in signal-to-noise ratio of > 10,000 times in liquid-state NMR. *Proc. Natl. Acad. Sci. U.S.A.* **100**, 10158–10163 (2003).
11. A. Abragam, M. Goldman, Principles of dynamic nuclear polarisation. *Rep. Prog. Phys.* **41**, 395–467 (1978).
12. K. N. Hu, G. T. Debelouchina, A. A. Smith, R. G. Griffin, Quantum mechanical theory of dynamic nuclear polarization in solid dielectrics. *J. Chem. Phys.* **134**, 125105 (2011).
13. H. Espinós, C. Munuera-Javaloy, I. Panadero, P. Acedo, R. Puebla, J. Casanova, E. Torrontegui, Enhancing polarization transfer from nitrogen-vacancy centers to external nuclear spins via dangling bond mediators. *Commun. Phys.* **7**, 42 (2024).
14. D. G. Mummy, E. A. Bier, Z. Wang, J. Korzekwinski, L. Morrison, C. Barkauskas, H. P. McAdams, R. M. Tighe, B. Driehuis, J. G. Mammarrappalli, Hyperpolarized 129Xe MRI and spectroscopy of gas-exchange abnormalities in nonspecific interstitial pneumonia. *Radiology* **301**, 211–220 (2021).
15. O. Doganay, T. Matin, M. Chen, M. Kim, A. McIntyre, D. R. McGowan, K. M. Bradley, T. Povey, F. V. Gleeson, Time-series hyperpolarized xenon-129 MRI of lobar lung ventilation of COPD in comparison to V/Q-SPECT/CT and CT. *Eur. Radiol.* **29**, 4058–4067 (2019).
16. K. Qing, N. J. Tustison, J. P. Mugler III, J. F. Mata, Z. Lin, L. Zhao, D. Wang, X. Feng, J. Y. Shin, S. J. Callahan, M. P. Bergman, K. Ruppert, T. A. Altes, J. M. Cassani, Y. M. Shim, Probing changes in lung physiology in COPD using CT, perfusion MRI, and hyperpolarized xenon-129 MRI. *Acad. Radiol.* **26**, 326–334 (2019).
17. S. Knecht, J. W. Blanchard, D. Barskiy, E. Cavallari, L. Dagys, E. Van Dyke, M. Tsukanov, B. Bliemel, K. Münnemann, S. Aime, F. Reineri, M. H. Levitt, G. Buntkowsky, A. Pines, P. Blümler, D. Budker, J. Eills, Rapid hyperpolarization and purification of the metabolite fumarate in aqueous solution. *Proc. Natl. Acad. Sci. U.S.A.* **118**, e2025383118 (2021).
18. A. B. Schmidt, J. Eills, L. Dagys, M. Gierse, M. Keim, S. Lucas, M. Bock, I. Schwartz, M. Zaitsev, E. Y. Chekmenev, S. Knecht, Over 20% carbon-13 polarization of perdeuterated pyruvate using reversible exchange with parahydrogen and spin-lock induced crossing at 50 μ T. *J. Phys. Chem. Lett.* **14**, 5305–5309 (2023).
19. M. Gierse, L. Nagel, M. Keim, S. Lucas, T. Speidel, T. Lobmeyer, G. Winter, F. Josten, S. Karaali, M. Fellermann, J. Scheuer, C. Müller, F. van Heijster, J. Skinner, J. Löffler, A. Parker, J. Handwerker, A. Marshall, A. Salhov, B. El-Kassem, C. Vassiliou, J. W. Blanchard, R. Picazo-Frutos, J. Eills, H. Barth, F. Jelezko, V. Rasche, F. Schilling, I. Schwartz, S. Knecht, Parahydrogen-polarized fumarate for preclinical in vivo metabolic magnetic resonance imaging. *J. Am. Chem. Soc.* **145**, 5960–5969 (2023).
20. T. R. Eichhorn, A. J. Parker, F. Josten, C. Müller, J. Scheuer, J. M. Steiner, M. Gierse, J. Handwerker, M. Keim, S. Lucas, M. U. Qureshi, A. Marshall, A. Salhov, Y. Qian, J. Binder, K. D. Jahnke, P. Neumann, S. Knecht, J. W. Blanchard, M. B. Plenio, F. Jelezko, L. Emsley, C. C. Vassiliou, P. Hautle, I. Schwartz, Hyperpolarized solution-state NMR spectroscopy with optically polarized crystals. *J. Am. Chem. Soc.* **144**, 2511–2519 (2022).
21. S. Tang, M. V. Meng, J. B. Slater, J. W. Gordon, D. B. Vigneron, B. A. Stohr, P. E. Z. Larson, Z. J. Wang, Metabolic imaging with hyperpolarized (13) C pyruvate magnetic resonance imaging in patients with renal tumors-Initial experience. *Cancer* **127**, 2693–2704 (2021).
22. T. H. Witney, M. I. Kettunen, D. E. Hu, F. A. Gallagher, S. E. Bohndiek, R. Napolitano, K. M. Brindle, Detecting treatment response in a model of human breast adenocarcinoma using hyperpolarised [1-13C]pyruvate and [1,4-13C2]fumarate. *Br. J. Cancer* **103**, 1400–1406 (2010).
23. E. M. Serrao, K. M. Brindle, Dynamic nuclear polarisation: The future of imaging in oncology? *Porto Biomed. J.* **2**, 71–75 (2017).
24. J. Kurhanewicz, D. B. Vigneron, J. H. Ardenkjaer-Larsen, J. A. Bankson, K. Brindle, C. H. Cunningham, F. A. Gallagher, K. R. Keshari, A. Kjaer, C. Laustsen, D. A. Mankoff, M. E. Merritt, S. J. Nelson, J. M. Pauly, P. Lee, S. Ronen, D. J. Tyler, S. S. Rajan, D. M. Spielman, L. Wald, X. Zhang, C. R. Malloy, R. Rizi, Hyperpolarized 13C MRI: Path to clinical translation in oncology. *Neoplasia* **21**, 1–16 (2019).
25. S. J. Nelson, J. Kurhanewicz, D. B. Vigneron, P. E. Larson, A. L. Harzstark, M. Ferrone, M. van Criekinge, J. W. Chang, R. Bok, I. Park, G. Reed, L. Carvajal, E. J. Small, P. Munster, V. K. Weinberg, J. H. Ardenkjaer-Larsen, A. P. Chen, R. E. Hurd, L. I. Odegardstuen, F. J. Robb, J. Tropp, J. A. Murray, Metabolic imaging of patients with prostate cancer using hyperpolarized [1-13C]pyruvate. *Sci. Transl. Med.* **5**, 198ra108 (2013).
26. J. H. Ardenkjaer-Larsen, A. M. Leach, N. Clarke, J. Urbahn, D. Anderson, T. W. Skloss, Dynamic nuclear polarization polarizer for sterile use intent. *NMR Biomed.* **24**, 927–932 (2011).
27. K. Golman, R. I. Zandt, M. Lerche, R. Pehrson, J. H. Ardenkjaer-Larsen, Metabolic imaging by hyperpolarized 13C magnetic resonance imaging for in vivo tumor diagnosis. *Cancer Res.* **66**, 10855–10860 (2006).
28. Z. J. Wang, M. A. Ohliger, P. E. Z. Larson, J. W. Gordon, R. A. Bok, J. Slater, J. E. Villanueva-Meyer, C. P. Hess, J. Kurhanewicz, D. B. Vigneron, Hyperpolarized (13)C MRI: State of the art and future directions. *Radiology* **291**, 273–284 (2019).
29. H. Allouche-Arnon, M. H. Lerche, M. Karlsson, R. E. Lenkinski, R. Katz-Brull, Deuteration of a molecular probe for DNP hyperpolarization—A new approach and validation for choline chloride. *Contrast Media Mol. Imaging* **6**, 499–506 (2011).
30. M. Carravetta, M. H. Levitt, Long-lived nuclear spin states in high-field solution NMR. *J. Am. Chem. Soc.* **126**, 6228–6229 (2004).
31. H. Allouche-Arnon, T. Wade, L. F. Waldner, V. N. Miller, J. M. Gomori, R. Katz-Brull, C. A. McKenzie, In vivo magnetic resonance imaging of glucose—Initial experience. *Contrast Media Mol. Imaging* **8**, 72–82 (2013).
32. M. H. Levitt, Long live the singlet state! *J. Magn. Reson.* **306**, 69–74 (2019).
33. B. Pokroy, J. P. Quintana, E. A. N. Caspi, A. Berner, E. Zolotoyabko, Anisotropic lattice distortions in biogenic aragonite. *Nat. Mater.* **3**, 900–902 (2004).
34. E. Seknazi, B. Pokroy, Residual strain and stress in biocrystals. *Adv. Mater.* **30**, e1707263 (2018).
35. I. Ben Shir, S. Kababya, I. Katz, B. Pokroy, A. Schmidt, Exposed and buried biomineral interfaces in the aragonitic shell of *Perna canaliculus* revealed by solid-state NMR. *Chem. Mater.* **25**, 4595–4602 (2013).
36. S. Borukhin, L. Bloch, T. Radlauer, A. H. Hill, A. N. Fitch, B. Pokroy, Screening the incorporation of amino acids into an inorganic crystalline host: The case of calcite. *Adv. Funct. Mater.* **22**, 4216–4224 (2012).
37. Y.-Y. Kim, J. D. Carloni, B. Demarchi, D. Sparks, D. G. Reid, M. E. Kunitake, C. C. Tang, M. J. Dier, C. L. Freeman, B. Pokroy, K. Penkman, J. H. Harding, L. A. Estroff, S. P. Baker, F. C. Meldrum, Tuning hardness in calcite by incorporation of amino acids. *Nat. Mater.* **15**, 903–910 (2016).
38. S. Mijowska, I. Polishchuk, A. Lang, E. Seknazi, C. Dejoie, S. Fermani, G. Falini, N. Demitri, M. Polentarutti, A. Katsman, B. Pokroy, High amino acid lattice loading at nonambient conditions causes changes in structure and expansion coefficient of calcite. *Chem. Mater.* **32**, 4205–4212 (2020).
39. K. W. Eberhardt, S. Mouaziz, G. Boero, J. Brugger, B. H. Meier, Direct observation of nuclear spin diffusion in real space. *Phys. Rev. Lett.* **99**, 227603 (2007).
40. A. Blank, A new approach to distance measurements between two spin labels in the > 10 nm range. *Phys. Chem. Chem. Phys.* **19**, 5222–5229 (2017).
41. N. Bloembergen, On the interaction of nuclear spins in a crystalline lattice. *Phys. Ther.* **15**, 386–426 (1949).
42. Y. Hovav, A. Feintuch, S. Vega, Dynamic nuclear polarization assisted spin diffusion for the solid effect case. *J. Chem. Phys.* **134**, 074509 (2011).
43. M. H. Levitt, *Spin Dynamics: Basics of Nuclear Magnetic Resonance* (Wiley, 2001).
44. C. P. Slichter, *Principles of Magnetic Resonance* (Springer Science & Business Media, 1990).
45. M. Ernst, B. Meier, “Spin diffusion in solids,” in *Studies in Physical and Theoretical Chemistry* (Elsevier, 1998), pp. 83–122.
46. B. Aharon, K. Itai, F. Akiva, “Method for preparation of highly polarized nuclear spins containing samples and uses thereof for NMR and MRI” US Patent 11,041,928 B2, June 2021 <https://patents.google.com/patent/US11041928B2/en> USPTO, Ed. (USA, 2020).
47. T. R. Eichhorn, Y. Takado, N. Salameh, A. Capozzi, T. Cheng, J. N. Hyacinthe, M. Mishkovsky, C. Roussel, A. Comment, Hyperpolarization without persistent radicals for in vivo real-time metabolic imaging. *Proc. Natl. Acad. Sci. U.S.A.* **110**, 18064–18069 (2013).
48. I. Katz, A. Feintuch, R. Carmieli, S. Markovic, K. Singh, T. Harris, L. Frydman, A. Blank, Dynamic nuclear polarization enhancement of 13C in glucose using electrical discharge induced radicals as polarizing agents. *J. Magn. Reson. Open* **10-11**, 100043 (2022).
49. L. Irving, The solubility of calcium in serum. *J. Biol. Chem.* **68**, 239–243 (1926).
50. Public registry of approved medicine, Calcium Gluconate 10% solution for injection/infusion BP (2024); <https://www.medicines.org.uk/emc/product/6264/smpc#ref> [Accessed 19 June 2024].
51. Y. Ueno, H. Futagawa, Y. Takagi, A. Ueno, Y. Mizushima, Drug-incorporating calcium carbonate nanoparticles for a new delivery system. *J. Control. Release* **103**, 93–98 (2005).

52. L. Dong, Y.-J. Xu, C. Sui, Y. Zhao, L.-B. Mao, D. Gebauer, R. Rosenberg, J. Avaro, Y.-D. Wu, H.-L. Gao, Z. Pan, H.-Q. Wen, X. Yan, F. Li, Y. Lu, H. Cölfen, S.-H. Yu, Highly hydrated paramagnetic amorphous calcium carbonate nanoclusters as an MRI contrast agent. *Nat. Commun.* **13**, 5088 (2022).
53. A. Som, R. Raliya, L. Tian, W. Akers, J. E. Ippolito, S. Singamaneni, P. Biswas, S. Achilefu, Monodispersed calcium carbonate nanoparticles modulate local pH and inhibit tumor growth in vivo. *Nanoscale* **8**, 12639–12647 (2016).
54. C. Wang, Z. Dong, Y. Hao, Y. Zhu, J. Ni, Q. Li, B. Liu, Y. Han, Z. Yang, J. Wan, K. Yang, Z. Liu, L. Feng, Coordination polymer-coated CaCO₃ reinforces radiotherapy by reprogramming the immunosuppressive metabolic microenvironment. *Adv. Mater.* **34**, e2106520 (2022).
55. F. J. Martin, K. Melnik, T. West, J. Shapiro, M. Cohen, A. A. Boiarski, M. Ferrari, Acute toxicity of intravenously administered microfabricated silicon dioxide drug delivery particles in mice: Preliminary findings. *Drugs R D* **6**, 71–81 (2005).
56. A. Lang, I. Polishchuk, G. Confalonieri, C. Dejoie, A. Maniv, D. Potashnikov, E. N. Caspi, B. Pokroy, Tuning the magnetization of manganese (II) carbonate by intracrystalline amino acids. *Adv. Mater.* **34**, e2201652 (2022).
57. L. Feng, Z. Dong, D. Tao, Y. Zhang, Z. Liu, The acidic tumor microenvironment: A target for smart cancer nano-theranostics. *Natl. Sci. Rev.* **5**, 269–286 (2017).
58. Health Encyclopedia, entry on Bicarbonate test (2024); <https://www.urmc.rochester.edu/encyclopedia/content.aspx?contenttypeid=167&contentid=bicarbonate> [Accessed 19 June 2024].
59. R. Ventura-Clapier, A. Garnier, V. Veksler, F. Joubert, Bioenergetics of the failing heart. *Biochim. Biophys. Acta* **1813**, 1360–1372 (2011).
60. L. Brečević, A. E. Nielsen, Solubility of amorphous calcium carbonate. *J. Cryst. Growth* **98**, 504–510 (1989).
61. A. Fitch, C. Dejoie, E. Covacci, G. Confalonieri, O. Grendal, L. Claustre, P. Guillou, J. Kieffer, W. de Nolf, S. Petitdemange, M. Ruata, Y. Watier, ID22—The high-resolution powder-diffraction beamline at ESRF. *J. Synchrotron Radiat.* **30**, 1003–1012 (2023).
62. K. Kouřil, M. Gramberg, M. Jurkatat, H. Kouřilová, B. Meier, A cryogen-free, semi-automated apparatus for bullet-dynamic nuclear polarization with improved resolution. *Magn. Reson.* **2**, 815–825 (2021).
63. K. Kouřil, H. Kouřilová, S. Bartram, M. H. Levitt, B. Meier, Scalable dissolution-dynamic nuclear polarization with rapid transfer of a polarized solid. *Nat. Commun.* **10**, 1733 (2019).
64. Y. Peng, H. Y. Sun, Z. C. Wang, X. D. Xu, J. C. Song, Z. J. Gong, Fabrication of alginate/calcium carbonate hybrid microparticles for synergistic drug delivery. *Chemotherapy* **61**, 32–40 (2015).
65. N. I. Hammadi, Y. Abba, M. N. M. Hezme, I. S. A. Razak, A. Z. Jaji, T. Isa, S. K. Mahmood, M. Zakaria, Formulation of a sustained release docetaxel loaded cockle shell-derived calcium carbonate nanoparticles against breast cancer. *Pharm. Res.* **34**, 1193–1203 (2017).

Acknowledgments: B.P. acknowledges the support of the Israel Discount Bank Academic Chair. We acknowledge the European Synchrotron Radiation Facility for the provision of beam time on ID22 (High-Resolution Powder X-Ray Diffraction Beamline) under proposal CH 6555. This paper is dedicated to the memory of our dear friend and colleague, the late professor A.S.

Funding: This work was partially supported by the Israel Innovation Authority (grant no. 67298) and the Technion Human Health Initiative (THHI), for the group of A.B. It was also supported by the Helmholtz Associations' Initiative and Networking (Impuls- und Vernetzungsfonds) Fund (grant VH-NG-1432) and received funding from the European Research Council (ERC) under the European Union's Horizon 2020 Research and Innovation program (grant agreement no. 951459), for the group of B.M.

Author contributions: All authors discussed the results and approved the manuscript. I.K. conceived the project and carried out the theoretical analysis. I.K., A.S., I.B.-S., K.K., B.M., A.C., A.L., B.P., and A.B. worked on the methodology. I.K. and A.L. prepared the materials. Funding was acquired by A.B., B.P., and B.M., who also supervised the research. Literature review and research steering was carried out by I.K. and M.J. The original draft was written by I.K., A.S., A.B., and B.M., and the final review and editing was carried out by all authors except A.S. (who passed away).

Competing interests: I.K., M.J., and A.B. are partly affiliated with a company "Beacon MRI" that submitted a pending patent application named "Particles for use in hyperpolarization" (application number US20220409748A1, filed on 23 June 2022, inventor: I.K.) related to the present paper. B.M. and K.K. are co-founders and co-owners of HyperSpin Scientific UG. The authors declare no other competing interests.

Data and materials availability: All data needed to evaluate the conclusions in the paper are present in the paper and/or the Supplementary Materials.

Submitted 24 January 2024

Accepted 6 June 2024

Published 12 July 2024

10.1126/sciadv.ado2483